



# Tailored thin film nanocomposite membrane incorporated with Noria for simultaneously overcoming the permeability-selectivity trade-off and the membrane fouling in nanofiltration process

Zhe Yang <sup>a,b</sup>, Longting Li <sup>c</sup>, Chi Jiang <sup>c</sup>, Na Zhao <sup>c</sup>, Shenghao Zhang <sup>b</sup>, Yaoli Guo <sup>b,c</sup>, Yi Chen <sup>b</sup>, Shuangmei Xue <sup>a,b</sup>, Chenhao Ji <sup>a,b</sup>, Shuzhen Zhao <sup>b</sup>, Ralph Rolly Gonzales <sup>d</sup>, Hideto Matsuyama <sup>d</sup>, Jianzhong Xia <sup>b</sup>, Q. Jason Niu <sup>a,b,\*</sup>

<sup>a</sup> College of Civil and Transportation Engineering, Shenzhen University, Shenzhen, 518061, China

<sup>b</sup> Institute for Advanced Study, Shenzhen University, Shenzhen, 518060, China

<sup>c</sup> State Key Laboratory of Heavy Oil Processing, China University of Petroleum (East China), Qingdao, 266580, China

<sup>d</sup> Research Center for Membrane and Film Technology, Department of Chemical Science and Engineering, Kobe University, 1-1 Rokkodai, Nada, Kobe, 657-8501, Japan



## ARTICLE INFO

### Keywords:

Noria  
Permeability-selectivity trade-off  
Antifouling  
Thin film nanocomposite membrane  
Nanofiltration

## ABSTRACT

Membrane fouling as well as the “trade-off effect” between water permeability and selectivity are the grand challenges for nanofiltration (NF) membranes. In this study, a macrocyclic molecule, Noria, was embedded in the polyamide layer to fabricate a thin film nanocomposite (TFN) membrane with high performances of separation and antifouling. Noria was first synthesized and dissolved in a piperazine (PIP) aqueous solution. Then the TFN membrane (i.e., PIP-Noria-TMC membrane, TMC is the abbreviation of 1,3,5-benzenetricarbonyl trichloride) was prepared by interfacial polymerization using PIP-Noria mixture as aqueous phase. The optimal PIP-Noria-TMC membrane reached  $147.6 \text{ L m}^{-2}\text{h}^{-1}\text{MPa}^{-1}$  of water permeability, which was almost twice that of the pristine NF membrane (i.e., PIP-TMC membrane). Meanwhile, the PIP-Noria-TMC membrane exhibited comparable  $\text{Na}_2\text{SO}_4$  rejection ( $\sim 98\%$ ) to the PIP-TMC membrane and outstanding mono/divalent salt selectivity. Besides, static adsorption tests using *E.coli* and bovine serum albumin (BSA) as the model foulants revealed that the surface of PIP-Noria-TMC membranes with high hydrophilicity and electronegative charge could effectively resist foulant attachment, which was also exhibited in the dynamic BSA filtration tests. Therefore, this work provided a practicable pathway to simultaneously overcome the permeability-selectivity trade-off and membrane fouling problems for the NF process.

## 1. Introduction

Besides the essential role of water for social development and human health, more than 30% of the global population does not have access to clean water today, and there is a prediction that the proportion will reach 60% in 2025 [1]. Hitherto, 2.5 billion people are in need of adequate sanitation, and the water-related disease causes the death of a child every minute [2]. Therefore, desalination of brackish water or reuse of wastewater is an effective way to address the water scarcity issue. Due to its high efficiency, environmentally friendly, and low operation cost, membrane technology is widely regarded as a promising technology for augmenting freshwater supply [3]. Nanofiltration (NF) membranes are typically polyamide (PA) thin film composite (TFC)

membranes fabricated by interfacial polymerization (IP) using piperazine (PIP) as aqueous phase and 1,3,5-benzenetricarbonyl trichloride (TMC) as organic phase. As a membrane technology between reverse osmosis (RO) and ultrafiltration (UF) in regard to pore size, NF membranes are capable of allowing water molecules and most of the monovalent ions to pass through, while rejecting multivalent ions and larger molecules [4]. Several exclusion forces including Donnan equilibrium, steric exclusion, and potentially dielectric exclusion exist at the interface between the NF membrane surface and the feed [5–8]. It can be seen that the NF technology can separate small molecules more effectively compared to UF and is less expensive to produce high-quality drinking water than RO [9,10]. Therefore, NF has attracted significant attention towards the treatment of drinking water over the past decades.

\* Corresponding author. Room 319, building NO. S, Yuehai campus, Shenzhen University, Shenzhen City, China.

E-mail address: [cjasonniu@szu.edu.cn](mailto:cjasonniu@szu.edu.cn) (Q.J. Niu).

As NF has the distinct advantages of sieving monovalent/divalent ions and small organic molecules with different molecular weight compared with UF and RO, extensive efforts are needed to further improve the selectivity of NF membranes. However, narrowing the pore size to enhance membrane selectivity is usually accompanied by a decline in water permeability. This “trade-off effect” between water permeability and selectivity is one of the pervasive and main obstacles that limit the further enhancement of NF membranes. Therefore, exploring NF membranes with both high water permeability and selectivity has become an important research topic to break the “trade-off effect”. On the one hand, the representative strategies for improving water permeability of membranes include making a thin selective layer, tailoring surface morphology to increase membrane effective area, improving membrane hydrophilicity, and reducing mass-transfer resistance [11–13]. On the other hand, membrane selectivity enhancement mainly involves in tuning pore size/pore size distribution and manipulating charge distribution [14]. Based on these knowledge, various membrane fabrication approaches have been successful for the enhancement of both water permeability and selectivity by tailoring desirable membrane properties. Particularly, the interlayer-thin film composite (i-TFC) membrane has been developed due to the formation of thinner PA layers with desired nanostructures, which significantly improves the water permeability and selectivity [15]. However, the fabrication process of the i-TFC membrane consists of constructing an interlayer on a support membrane by dip-coating polymeric materials or vacuum filtration with nanomaterials, and subsequently implementing IP. The extra interlayer coating process of i-TFC membranes results in the low reproducibility and capital cost problems for the industrial scaling-up [16]. Due to the simplicity and reliability, incorporating nanomaterials into the PA layer by one-step IP has become a promising route to get both ultra-permeable and highly selective TFC membranes, named as thin film nanocomposite (TFN) membrane. This concept proposed by Hoek et al. [17] has motivated many materials-oriented researches to explore the effect of various embedded nanomaterials such as carbon nanotube [18–20], graphene oxide [21], silica [22], silver [23], metal-organic frameworks (MOF) [24], zeolite nanoparticles [17,25], and polyhedral oligomeric silsesquioxane (POSS) [26] on the membrane performance. Several advantages of the TFN membrane contribute to overcoming the “trade-off effect”, including faster water transport within the porous nanomaterials, increased membrane affinity to water, and improved PA layer properties such as tunable charge density, pore structure, and thermal, chemical, and mechanical stability.

Another huge challenge of the NF membrane is the occurrence of membrane fouling. The organics and microorganisms in aqueous systems (e.g., wastewater, seawater et al.) may deposit and then aggregate on the membrane surface, which ultimately causes severe flux decline, increases operating pressure, and shortens the lifespan of NF membranes [27]. In general, membrane fouling is influenced by a nonspecific interaction between foulants and membrane surface properties. According to literatures, surface hydrophilicity as well as surface charge have major effect on membrane fouling. On the one hand, membrane surfaces with high hydrophilicity can prevent fouling effectively due to the formation of a hydration layer [28–30]. On the other hand, as most organics and microorganisms are negatively charged, membrane surfaces with neutral or negative charges are employed to repel the foulant attachment because of the electrostatic repulsion [31]. Therefore, both enhancing surface hydrophilicity and adjusting surface charge are effective strategies for improving the antifouling propensity of NF membranes.

Noria is a macrocyclic molecule, possessing 24 hydroxyl groups, 6 shallow cavities in the side, and a large central cavity. This well-defined pore structure of Noria could act as the water transport channel in the PA layer, meanwhile the plentiful hydroxyl groups could enhance membrane hydrophilicity and negative charge. Based on these advantages of Noria, tailoring a TFC membrane containing Noria might be effective for simultaneously overcoming the permeability-selectivity trade-off and

the membrane fouling in NF process. So far, Noria has been applied to construct an interlayer for i-TFC fabrication [32] and amination Noria has been synthesized to serve as the aqueous phase monomer alone in the IP process for TFC membrane preparation [33]. But there is no study on doping Noria into PIP aqueous phase for TFN membrane fabrication. In this study, we synthesized Noria by a one-pot condensation reaction of resorcinol and 1,5-pentanediol, and then the TFN NF membrane embedded with Noria (hereafter, called as “PIP-Noria-TMC membrane”) was prepared by one-step IP via doping Noria into the PIP aqueous phase. The effect of Noria doping concentration on membrane characterizations and performances was systematically investigated. The physicochemical properties of as-prepared membranes were characterized by Attenuated Total Reflection-Fourier Transform Infrared Spectroscopy (ATR-FTIR), water contact angle, and  $\zeta$ -potential. The membrane morphology was observed by scanning electron microscope (SEM) and atomic force microscope (AFM). For the membrane performance, the separation parameters of fabricated membranes including water permeability and salt rejection were tested in a crossflow system. The antifouling propensity of membranes was evaluated by static adsorption experiments as well as dynamic filtration tests.

## 2. Experimental

### 2.1. Materials

Polysulfone (PSF) UF membranes were used as the support film for IP process which were provided by Vontron Co., Ltd. (Beijing, China). PIP and TMC, two reactive monomers for IP, were purchased in Tokyo Chemical Industry (Tokyo, Japan). Resorcinol (Shanghai Adamas Reagent Co., Ltd., Shanghai, China) and glutaraldehyde (50% in water, Shanghai Aladdin Bio-Chem Technology Co., Ltd., Shanghai, China) were used to synthesize the Noria. *Escherichia coli* (*E.coli*) and bovine serum albumin (BSA, Sigma-Aldrich, St. Louis, MO, USA) were the model foulants for antifouling performance tests. Phosphate buffered saline (PBS, 1X, pH 7.4, Shanghai Adamas Reagent Co., Ltd.) was used as the solvent for BSA solution. Other chemicals, silver nitrate ( $\text{AgNO}_3$ ) was purchased from Sigma-Aldrich, while tryptone, hydrochloric acid (HCl, 37.0%), ethanol, hexane, methanol, sodium hydroxide (NaOH), sodium sulfate ( $\text{Na}_2\text{SO}_4$ ), magnesium sulfate ( $\text{MgSO}_4$ ), calcium chloride ( $\text{CaCl}_2$ ), and sodium chloride (NaCl), were obtained from Sinopharm Chemical Reagent Co., Ltd. (Shanghai, China). Milli-Q water was obtained in a water purification system (VIOMI, Foshan, China) for all the experiments.

### 2.2. Noria synthesis

Noria synthesis is based on a simple condensation reaction using resorcinol as a difunctional compound and glutaraldehyde as a tetrafunctional compound [34], which is illustrated in Fig. 1(a). Briefly, resorcinol (22 g) and 36.0% HCl (30 mL) were dissolved in ethanol (45 mL) at 80 °C with agitation and subsequently 50% glutaraldehyde (5 g) was dropwise added. After reacting for 48 h, adding the reaction mixture into methanol, and the precipitated product was rinse with Milli-Q water several times in a centrifuge (FC5816R, Ohaus, USA) with rotate speed of 4500 rpm, then thoroughly dried in freezing dry machine (Ningbo Scientz Biotechnology CO., Ltd., Ningbo, China) for 24 h. The final products were characterized by ATR-FTIR (NICOLET iS20, Thermo Fisher Scientific, U.S.A.) with wavenumber of 650 ~ 4000  $\text{cm}^{-1}$  and the  $^1\text{H}$  Nuclear Magnetic Resonance Spectroscopy ( $^1\text{H}$  NMR, Bruker AVANCE400, Germany) using  $\text{DMSO}-d_6$  as a deuterated solvent for sample preparation. This process of Noria synthesis slight modified the previous approach [29], which presents two advantages: (i) less toxic chemical usage. Instead of diethyl ether, Milli-Q water was used for product purification; (ii) Improved solubility of Noria product. Because Noria powder can be obtained by freeze-drying method. In the previous studies, however, the Noria product dried in oven with 60 °C became

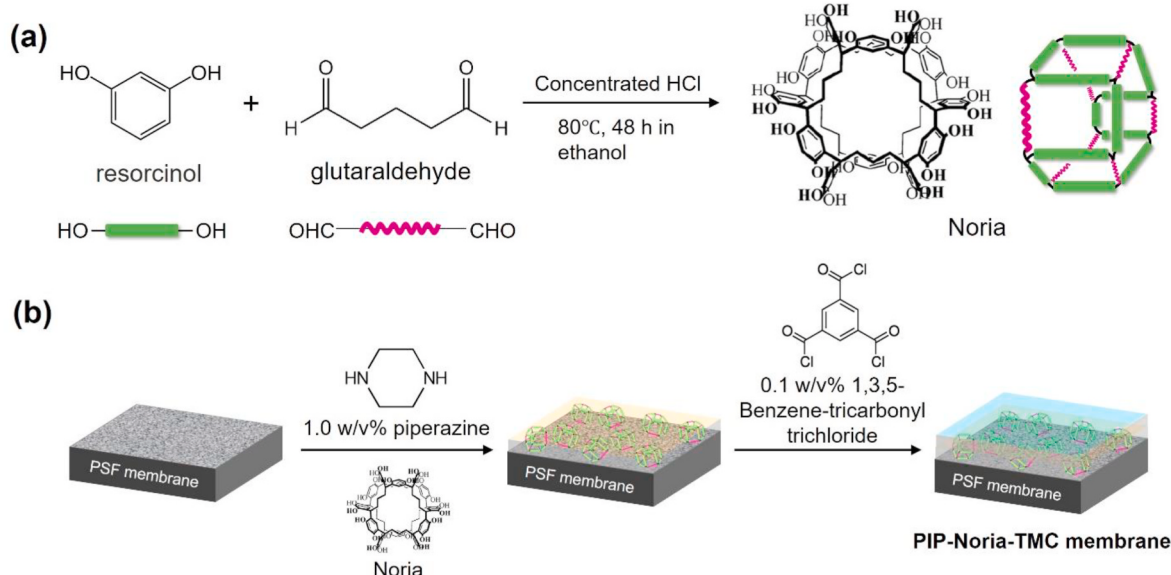


**Fig. 1.** (a) Condensation reaction of resorcinol and glutaraldehyde for Noria synthesis. (b) Scheme illustration of the fabrication of PIP-Noria-TMC membrane.

hard lumps with poor solubility.

### 2.3. Fabrication of PIP-Noria-TMC membrane

The fabrication procedure for PIP-Noria-TMC membrane was shown in Fig. 1(b). First, the PSF support film was dipped into a 1.0 w/v% PIP aqueous solution doped with different concentration of Noria for 2 min, after which the filter paper was used to completely remove the excess droplets on the support film. The applied Noria doping concentration consisted of 0.2, 0.4, 0.6, 0.8, and 1.0 w/v%. Secondly, to form a PA layer, a hexane solution containing 0.1 w/v% TMC was poured on the membrane surface for 2 min. Finally, the membrane was washed with hexane and heated at oven at 60 °C for 2 min. For the preparation of pristine NF membrane (hereafter, named as PIP-TMC membrane), it was identical to the aforementioned steps except for the absence of Noria. All the as-fabricated membranes were stored in Milli-Q water for further use.

### 2.4. Membrane characterizations

The chemical composition of PIP-TMC and PIP-Noria-TMC membranes was characterized by ATR-FTIR. The transmittance spectra with a resolution of 4 cm<sup>-1</sup> and wavenumber of 650 ~ 4000 cm<sup>-1</sup> were set up. Three locations of each membrane sample were measured and each location was scanned 16 times. Water contact angle measurements with time were carried out in drop shape analyzer (DSA25, Krüss, Germany) to evaluate the surface hydrophilicity of membranes. One measurement lasted 300 s. A microsyringe extruded a water droplet (4-μL) onto the membrane surface in the beginning, and a photograph was taken every second to evaluate the variation of water contact angle as a function of time. The water contact angle of membranes was determined at the end of the 300 s measurement process. In order to obtain the average data, at least five measurements were conducted for each membrane sample. Membrane surface charge was analyzed by ζ-potential measurements (SurPASSTM3, Anton paar, Austria) which was carried out from pH 3 to 9 using 1 mM KCl as the electrolyte solution. Three membranes of each sample were measured to confirm the repeatability. Membrane morphology was observed by SEM (Mira3 XMH, TESCAN, Czech) and AFM (L01F4C8, Bruker, Germany). Specifically, the thickness of PA layer was determined by the SEM micrographs of membrane cross-section, while the surface roughness parameters, including average

roughness ( $R_a$ ) and mean-square value ( $R_q$ ), were quantified by AFM micrographs of membrane surface with area of 5 μm × 5 μm. At least six micrographs were taken for each membrane sample to get the reliable value.

### 2.5. Membrane separation performance

Membrane separation parameters including water permeability and salt rejection were tested in a crossflow filtration system with effective membrane area of 18.5 cm<sup>2</sup>. Milli-Q water was fed to the membrane under an applied pressure of 0.5 MPa until the water permeability reached a stable state, and then the weight of permeate per minute was recorded to determine the water permeability. To evaluate the single salt rejection, four kinds of salt solutions including 2 g L<sup>-1</sup> Na<sub>2</sub>SO<sub>4</sub>, MgSO<sub>4</sub>, CaCl<sub>2</sub>, and NaCl were used as the feed solution. For both water permeability and salt rejection, at least 3 times measurements were carried out to ensure the reproducibility. The water permeability ( $J$ ), salt rejection ( $R$ ), and NaCl/Na<sub>2</sub>SO<sub>4</sub> selectivity ( $S_{NaCl/Na_2SO_4}$ ) were calculated by Eqs. (1)–(3), respectively [33]:

$$J = \frac{V}{S \times T \times P} \quad (1)$$

$$R = \frac{C_f - C_p}{C_f} \times 100\% \quad (2)$$

$$S_{NaCl/Na_2SO_4} = \frac{100 - R_{NaCl}}{100 - R_{Na_2SO_4}} \quad (3)$$

where  $V$  is the permeate volume,  $S$  is the effective membrane area,  $T$  is time, and  $P$  is the applied pressure;  $C_f$  and  $C_p$  are the salt concentration of feed and permeate, respectively, which were determined by an electric conductivity meter (B-771, Horiba, Kyoto, Japan).  $R_{NaCl}$  and  $R_{Na_2SO_4}$  are the rejection of NaCl and Na<sub>2</sub>SO<sub>4</sub>, respectively.

### 2.6. Antifouling propensity

#### 2.6.1. Static adsorption tests

Static adsorption tests were conducted using BSA and *E. coli* as the model protein and model bacteria, respectively. For the static BSA adsorption tests, the PIP-TMC and PIP-Noria-TMC membranes with area of 5 cm<sup>2</sup> were completely soaked into 5 mL 2 g L<sup>-1</sup> BSA solution using PBS (pH 7.4) as a solvent at 25 °C for 24 h. Afterwards, a 5 mL fresh PBS

solution was used to wash the unbound BSA from the membrane surface back to the BSA solution. The residual BSA amount in solution was analyzed through UV-vis spectrophotometer (UV-2600, Shimadzu, Japan) under the wavelength of 278 nm, while the surface of fouled membranes was observed by SEM. The BSA adsorption amount ( $Q$ ) of membranes was quantified by Eq. (4):

$$Q = \frac{V \times (c_0 - c_1)}{A} \quad (4)$$

where  $c_0$  and  $c_1$  are the BSA concentration before and after the static adsorption tests, respectively,  $V$  is the volume of BSA solution, and  $A$  is the membrane area.

The procedure of static bacterial adhesion tests was similar to the previous study [29]. Briefly, a colony of *E.coli* was transferred from a solid agar plate into tryptone broth and grown at 37 °C for 12 h with 120 rpm of shaken rate. Afterwards, 0.4 mL of bacterial suspension was transferred into a 20 mL fresh tryptone broth for a second culture for 4 h. By using the fresh tryptone broth, bacterial suspension was adjusted until the optical density at 600 nm (OD600) reached 1.0 (i.e.,  $\sim 10^9$  colony forming units per mL). To evaluate the antifouling propensity of membranes, a 0.5 cm × 1.0 cm membrane was contacted with 2 mL bacterial suspension at 25 °C with 100 rpm of shaken rate for 24 h. Afterwards, the unattached bacteria was removed from the membrane surface by rinsing the membrane with 0.85% NaCl aqueous solution, while the attached bacteria were first fixed on the membrane surface by soaking the membrane into 2.5% glutaraldehyde for 3 min and then observed under SEM. The percentage of bacterial coverage of each membrane sample was quantified from SEM micrographs by ImageJ software (National Institutes of Health, Bethesda, MD, USA) and the average data was obtained from five SEM micrographs of each membrane sample.

### 2.6.2. Dynamic filtration tests

The important evaluation method of the antifouling properties of membranes is dynamic filtration test which could simulate the NF process in practical applications. BSA was selected as the model foulant because proteins are ubiquitous foulants in typical feedwater sources [35]. First, membranes were set in a crossflow filtration system and filtrated with Milli-Q water. The initial water flux ( $J_0$ ) of each membrane was set as 150 L m<sup>-2</sup> h<sup>-1</sup> by adjusting the pressure. To initiate fouling, a feed solution containing 2 g L<sup>-1</sup> BSA was fed for 8 h, after which the fouled membranes were rinsed with Milli-Q water for 2 h. The water flux change of membranes was recorded by weighting the accumulate permeate every 2 h. The flux decline ratio ( $FDR$ ) and flux recovery ratio ( $FRR$ ) were quantified by Eq. (5) and Eq. (6), respectively.

$$FDR = \frac{J_0 - J_d}{J_0} \times 100\% \quad (5)$$

$$FRR = \frac{J_r}{J_0} \times 100\% \quad (6)$$

where  $J_0$  is the initial flux,  $J_d$  is the flux after 8-h BSA filtration, and  $J_r$  is the flux after 2-h water rinsing.

## 3. Results and discussion

### 3.1. Membrane characterizations

In this study, Noria was synthesized through a simple condensation reaction of resorcinol and glutaraldehyde, and this molecule is known to have a large central cavity with multi-hydroxyl groups. The chemical composition of the synthesized Noria was confirmed by ATR-FTIR and <sup>1</sup>H NMR as shown in Figs. S1(a) and S1(b). The solubility of Noria was demonstrated in Fig. S2. Precipitation appeared after 24 h when Noria was dissolved by water, which suggested that the Noria can be

suspended in water but is insoluble in water. In contrast, Noria could be easily dissolved in a NaOH solution with pH 13, indicating that Noria is soluble in an alkaline solution, which is consistent with the previous study [32,33]. In this case, as the PIP aqueous solution used for IP is also an alkaline solution with pH 13, Noria could be soluble and stable in the PIP aqueous solution (Fig. S2). Therefore, doping Noria in the PIP aqueous solution for IP is practical to incorporate Noria into the PA layer.

PIP-Noria-TMC membranes were fabricated by using TMC hexane solution as the organic phase and PIP-Noria aqueous solution as the aqueous phase. Chemical composition of the fabricated membranes was characterized by ATR-FTIR to access the existence of Noria. In Fig. 2(a), a peak at 1625 cm<sup>-1</sup> ascribed to the C=O stretching band of the amide appeared [26] in the ATR-FTIR spectra of PIP-TMC and PIP-Noria-TMC membranes due to the formation of PA layer by IP, which was absent in the spectrum of the PSF support film. In addition, the spectrum of the PIP-Noria-TMC membrane exhibited the characteristic peak of hydroxyl groups at 3140 ~ 3700 cm<sup>-1</sup>, suggesting the existence of Noria, that is, the successful incorporation of Noria into the PA layer. Notably, although the ester group could be generated by the reaction between the phenol hydroxyl group of Noria and the acyl chloride group of TMC [33], the reactivity of Noria molecules is much lower than PIP monomers. As a result, there was no peak at 1730 cm<sup>-1</sup> which represented the C=O stretching vibration of ester group in the ATR-FTIR spectrum of the PIP-Noria-TMC membrane. This inference was also supported by X-ray photoelectron spectroscopy (XPS) data. The molar ratio of oxygen and nitrogen ( $n[O]/n[N]$ ) as well as the molar ratio of carbon and nitrogen  $n[C]/n[N]$  increased after introducing Noria into the PA layer (Table S1). However, according to the peak deconvolution of the narrow-scan XPS spectra in Fig. S3(c) ~ S3(f), no ester group can be observed. Both ATR-FTIR and XPS data demonstrated that Noria can be effectively incorporated into the PA layer by a simple IP process without covalent reaction, that is, the non-covalent reaction would play a dominant role on the interaction between Noria molecules and PA network.

The effect of Noria doping concentration on chemical composition of the fabricated membranes was further investigated. As mentioned above, the broad peak between 3140 ~ 3700 cm<sup>-1</sup> in the ATR-FTIR spectrum belongs to the phenol hydroxyl group of Noria. Therefore, the PIP-Noria-TMC membranes with various Noria doping concentration were characterized by ATR-FTIR, whose spectra were focus on the wavenumber of 3100 ~ 3700 cm<sup>-1</sup>. In Fig. 2(b), the typical peak within 3140 ~ 3700 cm<sup>-1</sup> can be observed in all the ATR-FTIR spectra of PIP-Noria-TMC membranes but not in the spectrum of the PIP-TMC membrane, which further indicated the Noria was effectively introduced into the PA layer. Besides, with the increase of Noria doping concentration, the absorbance of the broad peak increased, representing the increase of Noria amount in the PA layer.

Moreover, as shown in Fig. 2(c), the surface color of the PIP-TMC membrane turned from white to yellow after the incorporation of Noria, which corresponds to the color of the synthesized Noria product (Fig. S1(a)). With the increase of Noria doping concentration, the membrane surface color turned from pale yellow to brighten yellow accordingly. After immersing in AgNO<sub>3</sub> aqueous solution for 24 h, the surface of PIP-Noria-TMC membranes became brown while there was no significant color change on the PIP-TMC membrane surface. This was ascribed to the in situ formation of silver nanoparticles (AgNPs) from which reduced Ag<sup>+</sup> ions by the phenol hydroxyl groups of Noria. By increasing the Noria doping concentration, the membrane surface color changed from light brown into dark brown, which was attributed to the increased loading of AgNPs resulting from the enhanced Noria content in the PA layer and thus increased concentration of phenol hydroxyl groups. These phenomena clearly illustrated the successful incorporation of Noria and the controllable Noria content in the PA layer by changing the Noria doping concentration.

Surface hydrophilicity was evaluated by water contact angle as shown in Fig. 3(a). Compared to the PIP-TMC membrane with water

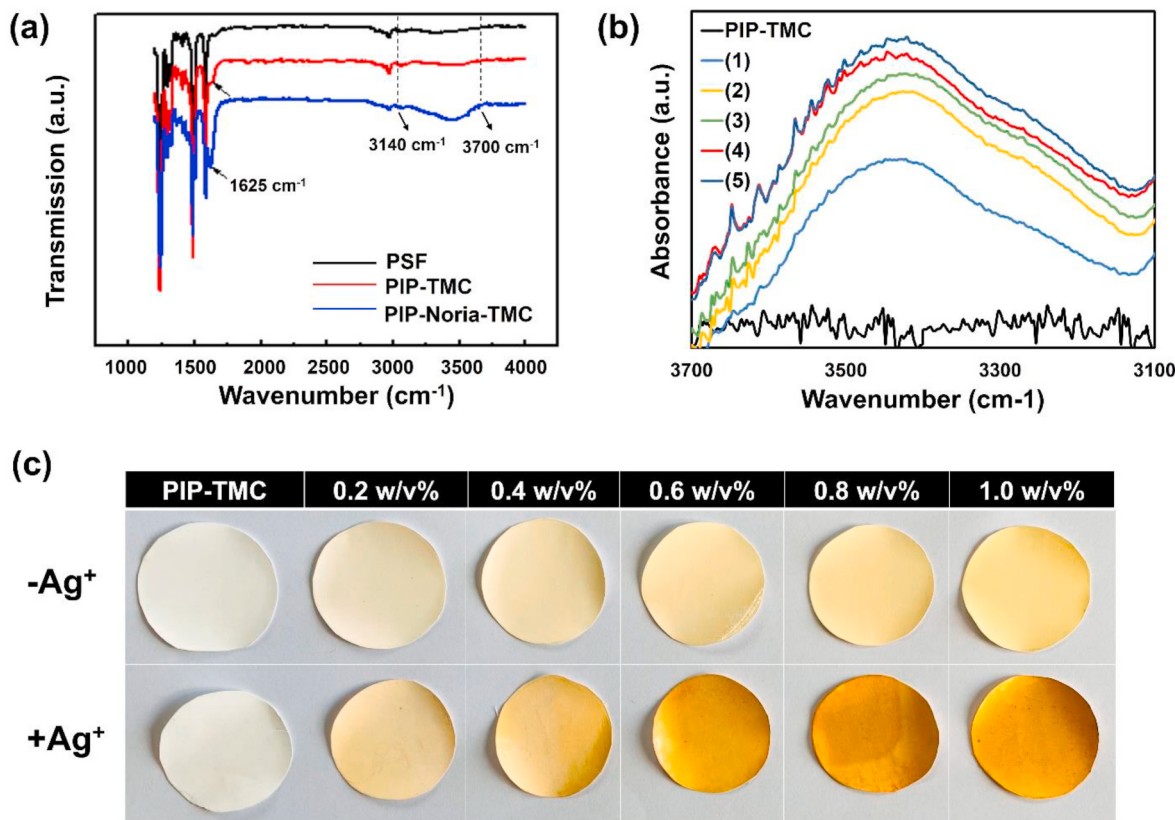


**Fig. 2.** (a) ATR-FTIR spectra of PSF support film, PIP-TMC membrane, and PIP-Noria-TMC membrane (The Noria doping concentration was 0.8 w/v%). (b) ATR-FTIR spectra (within the range of 3100 ~ 3700 cm<sup>-1</sup>) of PIP-TMC and PIP-Noria-TMC membranes with different Noria doping concentration, including (1) 0.2, (2) 0.4, (3) 0.6, (4) 0.8, and (5) 1.0 w/v%. (c) Observation of surface color of PIP-TMC and PIP-Noria-TMC membranes with different Noria doping concentration before and after  $\text{AgNO}_3$  treatment. (For interpretation of the references to color in this figure legend, the reader is referred to the Web version of this article.)

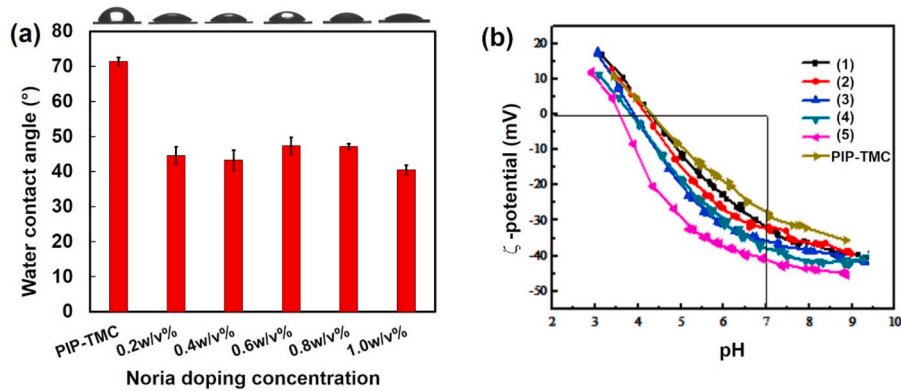


**Fig. 3.** (a) Water contact angle and (b)  $\zeta$ -potential of PIP-TMC and PIP-Noria-TMC membranes with various Noria doping concentration, including (1) 0.2, (2) 0.4, (3) 0.6, (4) 0.8, and (5) 1.0 w/v%.

contact angle of 71.4°, the PIP-Noria-TMC membranes showed lower water contact angle (40.4° ~ 47.1°) regardless of Noria doping concentration, which indicated the membrane surface became more hydrophilic after introducing Noria. However, among the PIP-Noria-TMC membranes, the change of Noria doping concentration had no significant effect on membrane surface hydrophilicity, indicating the hydrophilicity reached the limit. Besides, during the 300 s measurement process, the water contact angle of PIP-Noria-TMC membranes gradually decreased with time, while that of the PIP-TMC membrane fixed within ~20 s (Fig. S4). This further confirmed that the multi-hydroxyl group of Noria enhanced the membrane affinity to water.

In addition, membrane surface charge was assessed by  $\zeta$ -potential in

the range of pH 3 ~ 9. In Fig. 3(b), the  $\zeta$ -potential of PIP-TMC membrane changed from a positive value (~-10 mV) at pH 3.5 to a negative value (~-35 mV) at pH 9, whose isoelectric point (IEP) was at pH 4.3. Similar tendency of  $\zeta$ -potential was obtained after incorporating Noria into the PA layer, whereas the IEP gradually turned to left with the increase of Noria doping concentration. In other words, incorporation of Noria made the membrane surface charge become more negative because of the negative charge of multi-hydroxyl groups of Noria. Typically, when the pH is 7, the  $\zeta$ -potential value of PIP-TMC membrane was -27.5 mV while that of PIP-Noria-TMC membranes were lower than -31 mV.

### 3.2. Membrane morphology

The SEM and AFM micrographs were analyzed to study the influence of Noria doping concentration on membrane surface morphology, which were presented in Fig. 4. The PIP-TMC membrane depicted a traditional nodule structure (Fig. 4(a) and (g)). When the Noria doping concentration increased from 0.2 w/v% to 0.4 w/v%, these nodules were gradually buried as shown in SEM micrographs of Fig. 4(b) and (c). Meanwhile, the Ra decreased from 12.3 nm to 7.5 nm and the Rq decreased from 15.9 nm to 9.6 nm (Fig. 4(g)–(i)). Surprisingly, a wrinkled morphology started to appear on a surface of PIP-Noria-TMC membrane which fabricated using 0.6 w/v% of Noria doping concentration (Fig. 4(d)). Accordingly, the membrane surface became rougher since Ra and Rq increased to 10.3 nm and 13.7 nm, respectively (Fig. 4(j)). This wrinkled structure became more obvious and homogenous on the membrane surface fabricated using 0.8 w/v% Noria whose Ra and Rq reached 16.6 nm and 21.1 nm, respectively (Fig. 4(e) and (k)). However, the wrinkled structure was slightly buried when the Noria doping concentration reached 1.0 w/v% (Fig. 4(f)). As a result, the membrane surface became slightly smoother than the PIP-Noria-TMC membrane fabricated using 0.8 w/v% of Noria doping concentration (Fig. 4(l)).

In traditional IP process, the PIP monomers preserved within surface nanometer-sized pores of the support film can freely diffuse to the water-oil interface and subsequently react with TMC monomers in the organic phase [36], which generally produces a PA layer with the nodule structure. In contrast, using PIP-Noria mixture as aqueous phase in IP process reported herein could generate a PA layer with a wrinkled morphology, which showed the great importance of the macromolecule, Noria, to the formation of this unique structure. According to the estimation by the molecular dynamics simulation, when a certain amount of Noria molecules were added to the PIP aqueous solution, it interacted with the PIP monomers via the Van der Waals force or host-guest interaction (Figs. S5(a) and S5(c)) and the diffusion rate of PIP monomers was significantly reduced (Fig. S5(b)). Therefore, the synergistic effect of the physical obstruction (i.e., steric hindrance) and the chemical interaction (i.e., Van der Waals bonding or host-guest interaction) between PIP and Noria strongly restricts the diffusion of PIP monomers towards the water-oil interface during the IP process, leading to a diffusion-driven instability and generating a wrinkled morphology [37–40]. However, when the doping Noria concentration was too low to result in the appropriate diffusion differences of PIP and TMC monomers, no wrinkled structure appeared but the nodules became smaller compared to that of the PIP-TMC membrane (Fig. 4(a)–(c)). On the other hand, the wrinkled structure was denser but slightly buried in the presence of excess Noria content (Fig. 4(f)). Because the steric hindrance

was strengthened though, the aggregation of Noria turned to be stronger than the interaction between PIP monomers and Noria molecules, which weakened the influence of Noria molecules on the diffusion rate of the PIP monomers.

Cross-sections of membranes were observed by SEM to investigate the effect of Noria doping concentration on the thickness of PA layer. In Fig. 5, compared to the PIP-TMC membrane with 114 nm of PA layer thickness (Fig. 5(a)), thinner PA layers were obtained upon the incorporation of Noria (Fig. 5(b)–(f)). Specifically, the thickness of PA layer declined from 103 nm to 58 nm with the increase of Noria doping concentration from 0.2 w/v% to 0.8 w/v% (Fig. 5(b)–(e)). According to the Freger's study, the thickness of PA layer,  $\delta$ , can be estimated by the kinetic model for thin-film formation as shown in Eq. (7) [41]:

$$\delta \sim \left[ \frac{LD}{k(C_{fa} + C_{fb})} \right]^{1/3} \quad (7)$$

where  $L$  is the thickness of the diffusion boundary layer at the interface,  $D$  is the monomers diffusivity in the organic phase,  $k$  is the rate constant of the bimolecular reaction between the two monomers, and  $f_i$  is the functionality of monomer  $i$ .  $C_a$  and  $C_b$  is the equilibrium PIP concentration at the organic side of the interface and the TMC concentration in the organic phase, respectively. Eq. (7) implies that with the unchanged monomer concentration of PIP and TMC monomers, the decreased diffusion rate crossing the reaction interface leads to the reduce in PA layer thickness. Therefore, as discussed above, the diffusion rate of the PIP monomer was reduced by doping Noria (Fig. S5(b)). It means the monomer diffusivity,  $D$ , decreases in Eq. (7), the thickness of PA layer,  $\delta$ , is reasonably reduced. However, the thickness of PA layer slightly increased to 79 nm with 1.0 w/v% of Noria doping concentration (Fig. 5(f)). Such high density of Noria in PIP-Noria aqueous phase narrowed the distance between the neighboring Noria molecules and thus resulted in the aggregation of Noria. As a result, the PIP diffusion rate turned to be higher, causing a thicker PA layer.

### 3.3. Membrane separation performance

Water permeability of PIP-TMC and PIP-Noria-TMC membranes with different Noria doping concentration was tested using Milli-Q water as feed at 0.5 MPa and the data was displayed in Fig. 6(a). Compared to the PIP-TMC membrane with water permeability of  $77.5 \text{ L m}^{-2} \text{ h}^{-1} \text{ MPa}^{-1}$ , a maximum of 90% higher in water permeate property was obtained after incorporating Noria into the PA layer. Specifically, with increased Noria doping concentration from 0.2 w/v% to 0.8 w/v%, the water permeability was enhanced from  $101.2 \text{ L m}^{-2} \text{ h}^{-1} \text{ MPa}^{-1}$  to  $147.6 \text{ L m}^{-2} \text{ h}^{-1} \text{ MPa}^{-1}$ . In addition, the water permeability decreased with continually raising Noria doping concentration to 1.0 w/v%. This is mainly because the

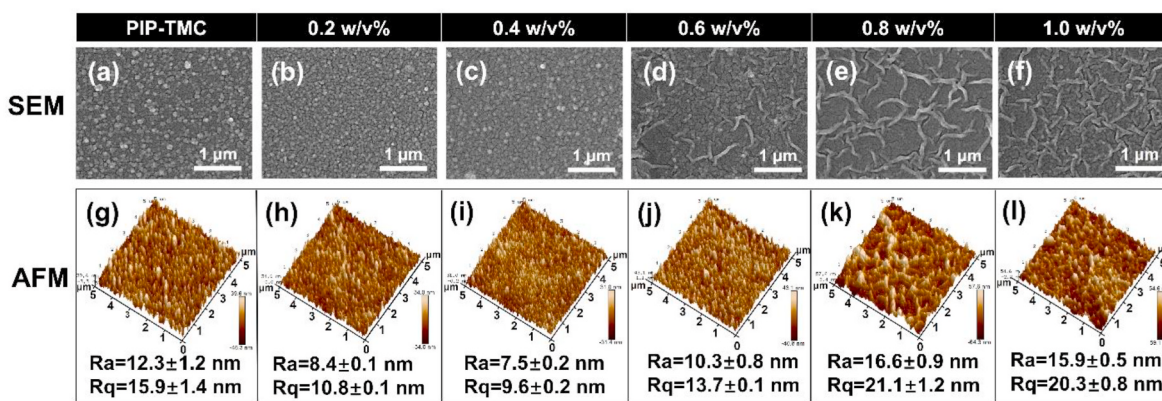


**Fig. 4.** SEM (a–f) and AFM (g–l) micrographs of surface morphology of (a, g) PIP-TMC and PIP-Noria-TMC membranes with various Noria doping concentration, including (b, h) 0.2, (c, i) 0.4, (d, j) 0.6, (e, k) 0.8, and (f, l) 1.0 w/v%. (the scale bar in SEM micrographs is 1  $\mu\text{m}$ ; the scale of AFM micrographs is 5  $\mu\text{m} \times 5 \mu\text{m}$ ; the data of Ra and Rq quantified from AFM micrographs were displayed below the AFM micrographs.)

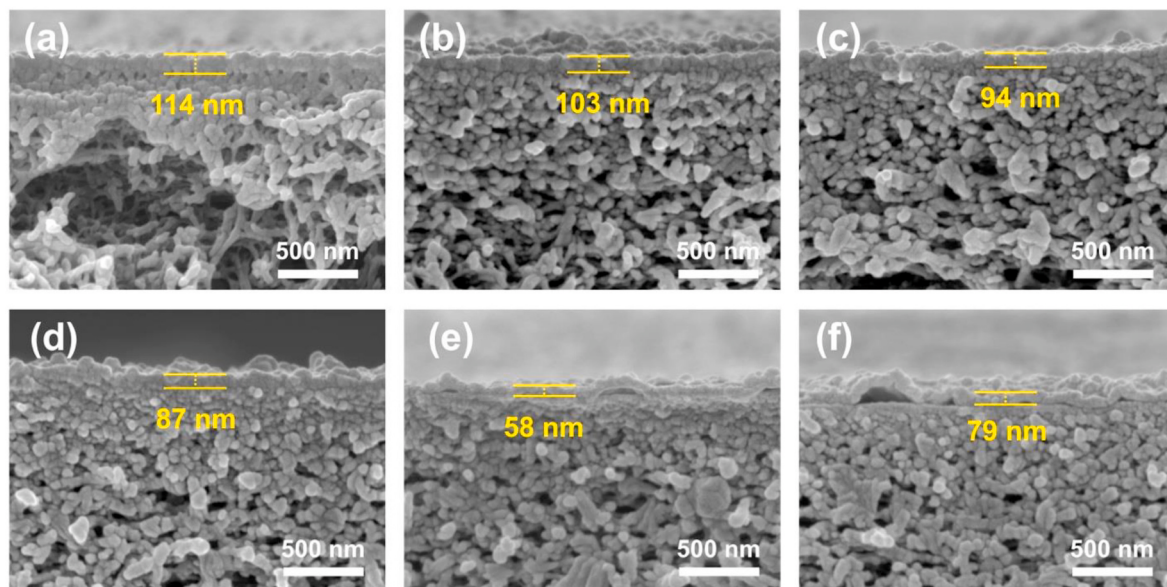


**Fig. 5.** Cross-sectional SEM micrographs of (a) PIP-TMC and PIP-Noria-TMC membranes with various Noria doping concentration, including (b) 0.2, (c) 0.4, (d) 0.6, (e) 0.8, and (f) 1.0 w/v%. (the scale bar in SEM micrographs is 500 nm; thickness data of PA layer are displayed inside the SEM micrographs.)

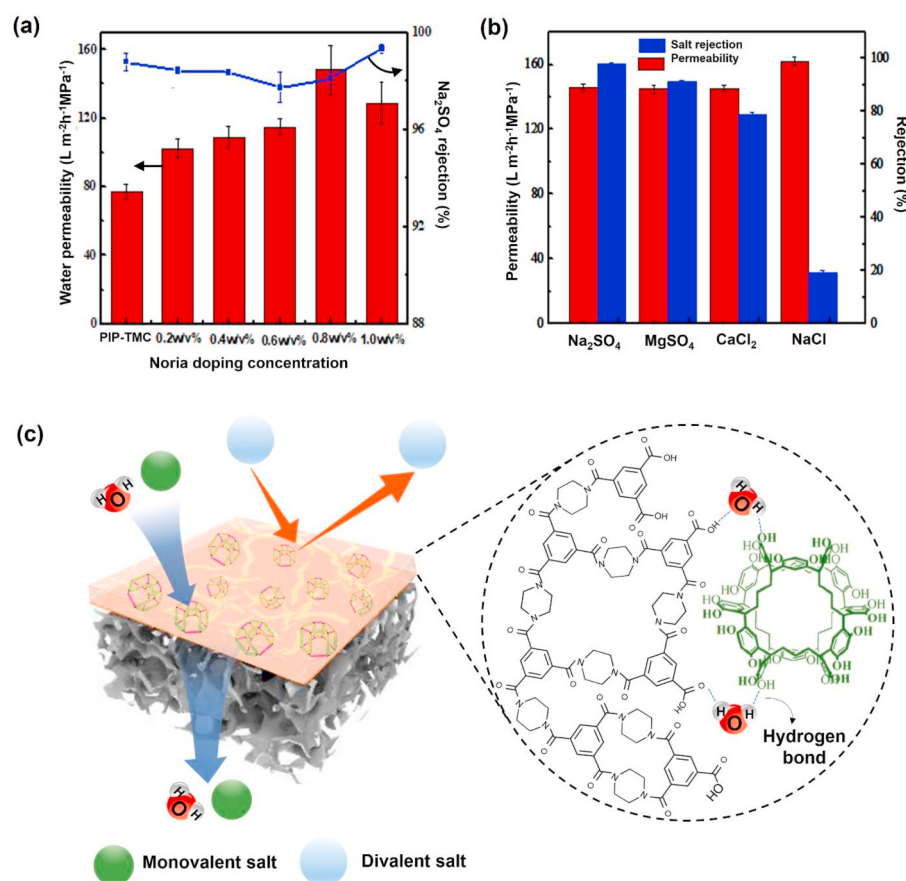


**Fig. 6.** (a) Water permeability and  $\text{Na}_2\text{SO}_4$  rejection of PIP-TMC and PIP-Noria-TMC membranes fabricated using different Noria doping concentration. (b) Salt solution permeability and salt rejection of the PIP-Noria-TMC membrane fabricated using 0.8 w/v% Noria. (c) Scheme of the separation behavior of PIP-Noria-TMC membranes.

slightly thicker PA layer (Fig. 5(f)) increased the transport resistance of water molecules. As for the  $\text{Na}_2\text{SO}_4$  rejection, under the optimal IP reaction time of 2 min (Fig. S6), PIP-Noria-TMC membranes presented comparable  $\text{Na}_2\text{SO}_4$  rejection (~98%) to PIP-TMC membranes,

indicating the incorporation of Noria has no damage to the PA layer. The result confirmed that 0.8 w/v% of Noria doping concentration is the optimal fabrication conditions of the PIP-Noria-TMC membrane, which exhibited higher water permeability and maintained high  $\text{Na}_2\text{SO}_4$

rejection.

The mechanism of this high water permeability was illustrated in Fig. 6(c). As discussed in section 3.2, because of the chemical interaction between PIP monomers and Noria molecules, the diffusion of PIP monomers from the aqueous phase to the organic phase was retarded by Noria molecules, which decelerated the IP reaction. As a result, the addition of Noria led to not only a decrease in PA layer thickness which can shorten the water molecule pathway, but also a wrinkled structure which effectively enlarges the actual surface area to contact with more water molecules passing through the interface. Moreover, carboxyl groups were naturally generated by hydrolysis of unreacted acyl chloride groups on TMC. We also speculated that both Noria as well as these carboxyl groups could bind with water molecules via hydrogen bonds (H-bond) so that the Noria molecules were able to adjacent to the PA layer through “H-bond-H<sub>2</sub>O-H-bond” interaction (Fig. 6(c)). The inherent structure of Noria with ~0.7 nm of the central cavity and ~0.5 nm of portal diameter [42] is bigger than the diameter of water molecules (~0.28 nm), which provides the transport channel for water molecules going through with low resistance. It can be seen that the incorporation of Noria into the PA layer contributed to thinner PA layers, larger surface area, and faster transport channels, jointly leading to higher water permeability of PIP-Noria-TMC membranes.

Separation performance of the optimal PIP-Noria-TMC membrane was further evaluated using four types of salts including Na<sub>2</sub>SO<sub>4</sub>, MgSO<sub>4</sub>, CaCl<sub>2</sub>, and NaCl. On the one hand, approximately 86% increase in salt solution permeability after incorporating 0.8 w/v% of Noria into the PA layer (Fig. S7), which was in accordance with the water permeability result (Fig. 6(a)). On the other hand, Fig. 6(b) presents the salt rejection as the following order: Na<sub>2</sub>SO<sub>4</sub> (98.3%) > MgSO<sub>4</sub> (91.2%) > CaCl<sub>2</sub> (79.6%) > NaCl (19.5%), which was a typical separation performance of NF membranes with negative charge [33]. Nevertheless, the mono/divalent selectivity (i.e., NaCl/Na<sub>2</sub>SO<sub>4</sub> selectivity) in this work shows superiority compared to other NF membranes [11,13,20,43–59] (Fig. 7), which could be explained by the Donnan exclusion theory and the size sieving. As the surface of PIP-Noria-TMC membranes were more negative charge (Fig. 3(b)), the strong electrostatic repulsion force existed between the divalent anions (i.e., SO<sub>4</sub><sup>2-</sup>) and the negative charged membranes, leading to high rejection of the divalent anion salts (i.e., Na<sub>2</sub>SO<sub>4</sub> and MgSO<sub>4</sub>). Compared to the Na<sub>2</sub>SO<sub>4</sub> rejection, the rejection of MgSO<sub>4</sub> and CaCl<sub>2</sub> was lower because of the stronger electrostatic attraction force between the divalent cations (i.e., Mg<sup>2+</sup> and Ca<sup>2+</sup>) and the negative charged membranes. Furthermore, as the

hydrated radius of Ca<sup>2+</sup> (4.12 Å) is smaller than that of Mg<sup>2+</sup> (4.28 Å) [60], the rejection of CaCl<sub>2</sub> was lower than that of MgSO<sub>4</sub>. In addition, the lowest rejection of NaCl was ascribed to the relatively weak electrostatic repulsion force between the monovalent anions (i.e., Cl<sup>-</sup>) and the negative charged membranes, as well as the smaller hydrated radius of Na<sup>+</sup> (3.58 Å) [60].

In summary, the results above demonstrated that the existence of Noria in the PA layer not only improves the water permeability, but also accurately separates mono/divalent salt with high divalent salt rejection. Therefore, the PIP-Noria-TMC membrane shows a high potential for coordinating the “trade-off effect” between water permeability and selectivity for NF membranes.

### 3.4. Antifouling performance of PIP-Noria-TMC membranes

Static adsorption tests were carried out to evaluate the antifouling performance of PIP-Noria-TMC membranes, using *E.coli* as the model bacteria foulant and BSA as the model protein foulant. The data of static bacterial adhesion test was shown in Fig. 8(a). Compared with PIP-TMC membranes, the PIP-Noria-TMC membranes showed ~90% reduction in the fraction of surface area covered by *E.coli*. Furthermore, the SEM micrographs of PIP-TMC and PIP-Noria-TMC membranes after static bacterial adhesion were shown in Fig. 8(c). The area covered by *E.coli* was highlighted in green. It is obvious that the surface of PIP-Noria-TMC membranes exhibited much less green area than the PIP-TMC membrane, indicating the antifouling propensity was significantly improved after introducing Noria into the PA layer. Similar tendency was obtained in the static BSA adsorption tests as shown in Fig. 8(b). The BSA adsorption amount of the PIP-TMC membrane decreased from 376.6 µg/cm<sup>2</sup> to <90 µg/cm<sup>2</sup> after the addition of Noria, which was evidently observed in SEM micrographs in Fig. 8(c).

According to the results of separation performance in section 3.3 and static adsorption tests above, PIP-Noria-TMC membranes fabricated by using 0.8 w/v% of Noria doping concentration integrated high water permeability, selectivity, and resistance of foulant attachment. Therefore, this membrane was selected to continue the evaluation of anti-fouling propensity by dynamic BSA filtration tests. Fig. 9(a) presents the water flux variation of PIP-TMC and PIP-Noria-TMC membranes during the dynamic BSA filtration tests consisting of 8-h BSA filtration and 2-h water cleaning. The FDR after BSA filtration and FRR after water cleaning were analyzed in Fig. 9(b). In Fig. 9(a), during 8-h BSA filtration, the water flux variation of PIP-TMC and PIP-Noria-TMC membrane showed a similar tendency to each other in the beginning of 6 h, which decreased from 150 L m<sup>-2</sup>h<sup>-1</sup> to ~138 L m<sup>-2</sup>h<sup>-1</sup>. Afterwards, the water flux of PIP-TMC membrane continually decline to 115 L m<sup>-2</sup>h<sup>-1</sup>, while there was no significant change on the water flux of PIP-Noria-TMC membrane. This phenomenon clearly suggested that the PIP-Noria-TMC membrane exhibited excellent antifouling properties against BSA, which was also demonstrated by the lower FDR of PIP-Noria-TMC membrane (10%) than that of PIP-TMC membrane (23%) (Fig. 9(b)). Moreover, after the fouled membranes were cleaned by water flushing, almost 95% water flux of PIP-Noria-TMC membrane could be recovered, which was much higher than the FRR of PIP-TMC membrane (78%). It indicated the attached BSA was easily removed from the surface of PIP-Noria-TMC membrane by water flushing, while the fouled PIP-TMC membrane was difficult to be cleaned. These results demonstrated that the antifouling propensity of NF membranes was effectively improved by the incorporation of Noria. Nevertheless, it can be seen that the strategies of enhancing membrane hydrophilicity as well as adjusting surface charge still inevitably succumb to fouling eventually, necessitating cleaning. More optimal design and modification are needed to further improve the fouling mitigation, such as the incorporation of photocatalytic materials into membranes for foulant degradation [61].

The improved antifouling propensity of PIP-Noria-TMC membranes described above could partly be credited to the combined high hydrophilicity and negative charge surfaces contributed by the addition of

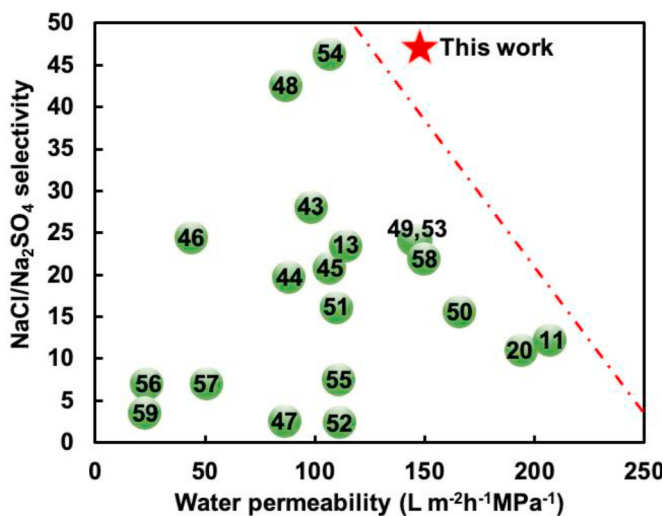
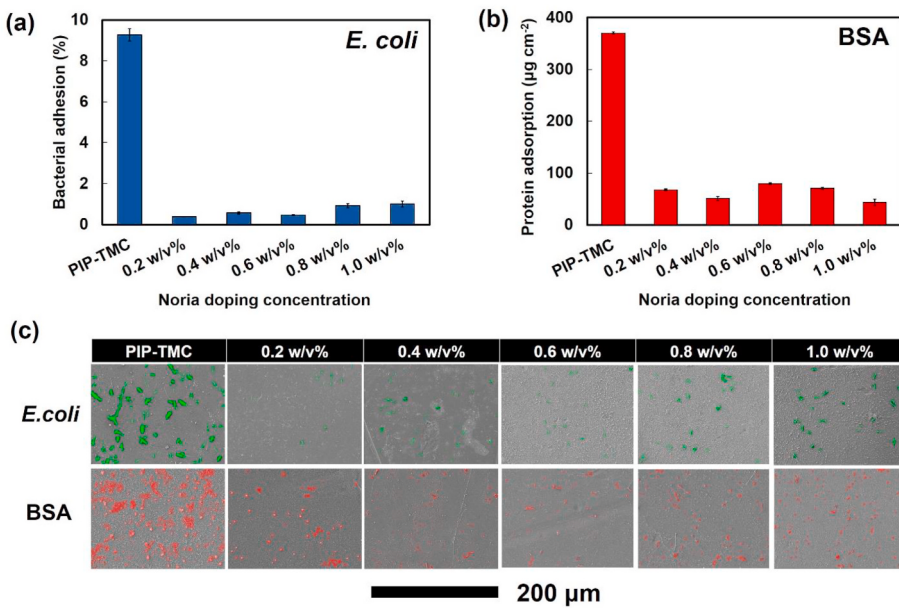
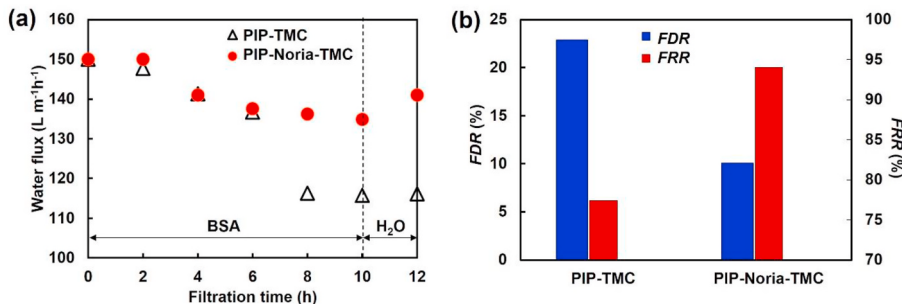


Fig. 7. NaCl/Na<sub>2</sub>SO<sub>4</sub> selectivity comparison between this work and other NF membranes referred to ref. [11,13,20,43–59]. (The number marked in each point means the reference number.)



**Fig. 8.** Data of static adsorption tests using (a) *E. coli* and (b) BSA as the model foulants. (c) SEM micrographs of PIP-TMC and PIP-Noria-TMC membranes after static adsorption tests (The area covered by *E.coli* and BSA was highlighted in green and red, respectively). (For interpretation of the references to color in this figure legend, the reader is referred to the Web version of this article.)



**Fig. 9.** (a) Water flux of PIP-TMC and PIP-Noria-TMC membranes as a function of filtration time during dynamic BSA filtration tests; (b) Flux decline ratio (FDR) and flux recovery ratio (FRR) of PIP-TMC and PIP-Noria-TMC membranes. (The PIP-Noria-TMC membrane tested in dynamic BSA filtration tests was fabricated using 0.8 w/v% Noria.)

Noria. As a result of water contact angle in Fig. 3(a), the addition of Noria with multi-hydroxyl groups equipped the membrane with higher hydrophilicity. It could facilitate the formation of a strong hydration layer which obstructed the direct contact between the foulants and the membrane surface. On the other hand, the *E.coli* and BSA foulants were negative charged at pH 7 [35]. Because the data of  $\zeta$ -potential in Fig. 3(b) confirmed that the incorporation of Noria molecules made the membrane surface become more negative charge, it enhanced the electrostatic repulsion between the anionic foulants and the membrane surface and led to the better antifouling propensity of PIP-Noria-TMC membranes.

#### 4. Conclusion

In this study, a PIP-Noria-TMC membrane integrating excellent separation performance and antifouling propensity was prepared by a one-step IP process using PIP-Noria mixture as the aqueous phase. Noria was successfully synthesized and soluble in the PIP aqueous solution. The incorporation content of Noria in the PA layer was controllable by adjusting the Noria doping concentration in the PIP-Noria aqueous phase. The optimal PIP-Noria-TMC membrane reached  $147.6 \text{ L m}^{-2}\text{h}^{-1}\text{MPa}^{-1}$  of water permeability, which was almost twice that of PIP-TMC

membranes. Meanwhile, the PIP-Noria-TMC membrane exhibited comparable  $\text{Na}_2\text{SO}_4$  rejection to PIP-TMC membrane and outstanding mono/divalent salt selectivity. The intensified water permeability was credited to the incorporation of Noria into the PA layer. On the one hand, the diffusion rate of PIP was decelerated by the addition of Noria during IP process, which endowed the membrane with a thinner PA layer and larger actual surface area (i.e., wrinkled structure) to facilitate the passage of water molecules. On the other hand, the cavity of embedded Noria in the PA layer could act as water transport channels to further improve the water permeability. Furthermore, as both surface hydrophilicity and electronegativity of membranes were remarkably enhanced after the addition of Noria molecules, the PIP-Noria-TMC membranes reached ~90% reduction on bacterial adhesion and ~75% decline in BSA adsorption, exhibiting much higher resistance for foulants compared with PIP-TMC membranes. During the dynamic BSA filtration test, the PIP-Noria-TMC membrane exhibited lower water flux decline and higher water flux recovery than PIP-TMC membranes. Taken together, this PIP-Noria-TMC membrane offers an effective route to simultaneously overcome the permeability-selectivity trade-off and membrane fouling problems, providing a great potential for use in wastewater treatment and desalination by NF technology.

## Author contributions

**Zhe Yang:** Conceptualization, Methodology, Writing-Original draft, Funding acquisition.  
**Longting Li:** Investigation, Formal analysis.  
**Chi Jiang:** MD simulation operation.  
**Na Zhao:** Investigation.  
**Shenghao Zhang:** Investigation.  
**Yaoli Guo:** Visualization.  
**Yi Chen:** Investigation.  
**Shuangmei Xue:** Visualization.  
**Chenhao Ji:** Software, Data Curation.  
**Shuzhen Zhao:** Resources.  
**Ralph Rolly Gonzales:** Writing - Review & Editing.  
**Hideto Matsuyama:** Writing - Review & Editing.  
**Jianzhong Xia:** Project administration.  
**Q. Jason Niu:** Funding acquisition, Supervision, Writing - Review & Editing.

## Declaration of competing interest

The authors declare that they have no known competing financial interests or personal relationships that could have appeared to influence the work reported in this paper.

## Acknowledgements

The authors would like to acknowledge the National Natural Science Foundation of China (NO. U2006230) and the China Postdoctoral Science Foundation (NO. 2021M692190) for the financial support.

## Appendix A. Supplementary data

Supplementary data to this article can be found online at <https://doi.org/10.1016/j.memsci.2021.119863>.

## References

- [1] R.F. Service, Desalination freshens up, *Science* 313 (2006) 1088–1090.
- [2] M.S. Mahmud, S.M.A. Amin, M.A.W. Rashed, R. Mahmud, Water, sanitation and hygiene practices among ethnic communities in Chittagong Hill Tracts, Bangladesh, *Int. J. Curr. Res. 12* (2020) 13269–13275.
- [3] C.Y. Tang, Z. Yang, H. Guo, J.J. Wen, L.D. Nghiem, E. Cornelissen, Potable water reuse through advanced membrane technology, *Environ. Sci. Technol.* 52 (2018) 10215–10223.
- [4] X. Chen, M. Qiu, H. Ding, K. Fu, Y. Fan, A reduced graphene oxide nanofiltration membrane intercalated by well-dispersed carbon nanotubes for drinking water purification, *Nanoscale* 8 (2016) 5696–5705.
- [5] J. Palmeri, J. Sandeaux, R. Sandeaux, X. Lefebvre, P. David, C. Guizard, P. Amblard, J.-F. Diaz, B. Lamaze, Modeling of multi-electrolyte transport in charged ceramic and organic nanofilters using the computer simulation program NanoFlux, *Desalination* 147 (2002) 231–236.
- [6] X. Lefebvre, J. Palmeri, J. Sandeaux, R. Sandeaux, P. David, B. Maleyre, C. Guizard, P. Amblard, J.-F. Diaz, B. Lamaze, Nanofiltration modeling: a comparative study of the salt filtration performance of a charged ceramit membrane and an organic nanofilter using the computer simulation program NANOFUX, *Separ. Purif. Technol.* 32 (2003) 117–126.
- [7] C. Mazzoni, F. Orlandini, S. Bandini, Role of electrolyte type on  $TiO_2-ZrO_2$  nanofiltration membranes performances, *Desalination* 240 (2009) 227–235.
- [8] X. Chen, W. Zhang, Y. Lin, Y. Cai, M. Qiu, Y. Fan, Preparation of high-flux  $\gamma$ -alumina nanofiltration membranes by using a modified sol-gel method, *Microporous Mesoporous Mater.* 214 (2015) 195–203.
- [9] F.C. Kramer, R. Shang, S.G. Heijman, S.M. Scherrenberg, J.B. van Lier, L. C. Rietveld, Direct water reclamation from sewage using ceramic tight ultra-and nanofiltration, *Separ. Purif. Technol.* 147 (2015) 329–336.
- [10] X. Da, J. Wen, Y. Lu, M. Qiu, Y. Fan, An aqueous sol-gel process for the fabrication of high-flux YSZ nanofiltration membranes as applied to the nanofiltration of dye wastewater, *Separ. Purif. Technol.* 152 (2015) 37–45.
- [11] M. Wu, J. Yuan, H. Wu, Y. Su, H. Yang, X. You, R. Zhang, X. He, N.A. Khan, R. Kasher, Ultrathin nanofiltration membrane with polydopamine-covalent organic framework interlayer for enhanced permeability and structural stability, *J. Membr. Sci.* 576 (2019) 131–141.
- [12] C. Jiang, L. Tian, Z. Zhai, Y. Shen, W. Dong, M. He, Y. Hou, Q.J. Niu, Thin-film composite membranes with aqueous template-induced surface nanostructures for enhanced nanofiltration, *J. Membr. Sci.* 589 (2019) 117244.
- [13] W. Shang, F. Sun, W. Jia, J. Guo, S. Yin, P.W. Wong, A.K. An, High-performance nanofiltration membrane structured with enhanced stripe nano-morphology, *J. Membr. Sci.* 600 (2020) 117852.
- [14] H. Zhang, Q. He, J. Luo, Y. Wan, S.B. Darling, Sharpening nanofiltration: strategies for enhanced membrane selectivity, *ACS Appl. Mater. Interfaces* 12 (2020) 39948–39966.
- [15] Z. Yang, P.-F. Sun, X. Li, B. Gan, L. Wang, X. Song, H.-D. Park, C.Y. Tang, A critical review on thin-film nanocomposite membranes with interlayered structure: mechanisms, recent developments, and environmental applications, *Environ. Sci. Technol.* 54 (2020) 15563–15583.
- [16] C. Ji, Z. Zhai, C. Jiang, P. Hu, S. Zhao, S. Xue, Z. Yang, T. He, Q.J. Niu, Recent advances in high-performance TFC membranes: a review of the functional interlayers, *Desalination* 500 (2020) 114869.
- [17] B.-H. Jeong, E.M. Hoek, Y. Yan, A. Subramani, X. Huang, G. Hurwitz, A.K. Ghosh, A. Jawor, Interfacial polymerization of thin film nanocomposites: a new concept for reverse osmosis membranes, *J. Membr. Sci.* 294 (2007) 1–7.
- [18] J. nan Shen, C. chao Yu, H. min Ruan, C. jie Gao, B. Van der Bruggen, Preparation and characterization of thin-film nanocomposite membranes embedded with poly (methyl methacrylate) hydrophobic modified multiwalled carbon nanotubes by interfacial polymerization, *J. Membr. Sci.* 442 (2013) 18–26.
- [19] S.-M. Xue, Z.-L. Xu, Y.-J. Tang, C.-H. Ji, Polypiperazine-amide nanofiltration membrane modified by different functionalized multiwalled carbon nanotubes (MWNTS), *ACS Appl. Mater. Interfaces* 8 (2016) 19135–19144.
- [20] Z. Liao, X. Fang, J. Xie, Q. Li, D. Wang, X. Sun, L. Wang, J. Li, Hydrophilic hollow nanocube-functionalized thin film nanocomposite membrane with enhanced nanofiltration performance, *ACS Appl. Mater. Interfaces* 11 (2019) 5344–5352.
- [21] S. Bano, A. Mahmood, S.-J. Kim, K.-H. Lee, Graphene oxide modified polyamide nanofiltration membrane with improved flux and antifouling properties, *J. Mater. Chem. A* 3 (2015) 2065–2071.
- [22] V. Vatanpour, M. Kavian, Synergistic effect of silica nanoparticles in the matrix of a poly (ethylene glycol) diacrylate coating layer for the surface modification of polyamide nanofiltration membranes, *J. Appl. Polym. Sci.* 133 (2016) 43793.
- [23] S.Y. Lee, H.J. Kim, R. Patel, S.J. Im, J.H. Kim, B.R. Min, Silver nanoparticles immobilized on thin film composite polyamide membrane: characterization, nanofiltration, antifouling properties, *Polym. Adv. Technol.* 18 (2007) 562–568.
- [24] Q. Li, Z. Liao, J. Xie, L. Ni, C. Wang, J. Qi, X. Sun, L. Wang, J. Li, Enhancing nanofiltration performance by incorporating tannic acid modified metal-organic frameworks into thin-film nanocomposite membrane, *Environ. Res.* 191 (2020) 110215.
- [25] J. Duan, Y. Pan, F. Pacheco, E. Litwiller, Z. Lai, I. Pinna, High-performance polyamide thin-film-nanocomposite reverse osmosis membranes containing hydrophobic zeolitic imidazolate framework-8, *J. Membr. Sci.* 476 (2015) 303–310.
- [26] X. You, T. Ma, Y. Su, H. Wu, M. Wu, H. Cai, G. Sun, Z. Jiang, Enhancing the permeation flux and antifouling performance of polyamide nanofiltration membrane by incorporation of PEG-POSS nanoparticles, *J. Membr. Sci.* 540 (2017) 454–463.
- [27] L. Ren, J. Chen, Q. Lu, J. Han, H. Wu, Antifouling nanofiltration membrane fabrication via surface assembling light-responsive and regenerable functional layer, *ACS Appl. Mater. Interfaces* 12 (2020) 52050–52058.
- [28] Z. Yang, D. Saeki, R. Takagi, H. Matsuyama, Improved anti-biofouling performance of polyamide reverse osmosis membranes modified with a polyampholyte with effective carboxyl anion and quaternary ammonium cation ratio, *J. Membr. Sci.* 595 (2020) 117529.
- [29] Z. Yang, D. Saeki, H. Matsuyama, Zwitterionic polymer modification of polyamide reverse-osmosis membranes via surface amination and atom transfer radical polymerization for anti-biofouling, *J. Membr. Sci.* 550 (2018) 332–339.
- [30] Z. Yang, D. Saeki, H.-C. Wu, T. Yoshioka, H. Matsuyama, Effect of polymer structure modified on RO membrane surfaces via surface-initiated ATRP on dynamic biofouling behavior, *J. Membr. Sci.* 582 (2019) 111–119.
- [31] Z. Yang, R. Takagi, X. Zhang, T. Yasui, L. Zhang, H. Matsuyama, Engineering a dual-functional sulfonated polyelectrolyte-silver nanoparticle complex on a polyamide reverse osmosis membrane for robust biofouling mitigation, *J. Membr. Sci.* 618 (2021) 118757.
- [32] Z. Zhai, C. Jiang, N. Zhao, W. Dong, H. Lan, M. Wang, Q.J. Niu, Fabrication of advanced nanofiltration membranes with nanostrand hybrid morphology mediated by ultrafast Noria-polyethyleneimine codeposition, *J. Mater. Chem. A* 6 (2018) 21207–21215.
- [33] L. Ren, J. Chen, Q. Lu, C. Wang, J. Han, K. Huang, X. Pan, H. Wu, Construction of high selectivity and antifouling nanofiltration membrane via incorporating macrocyclic molecules into active layer, *J. Membr. Sci.* 597 (2020) 117641.
- [34] H. Kudo, R. Hayashi, K. Mitani, T. Yokozawa, N.C. Kasuga, T. Nishikubo, Molecular waterwheel (Noria) from a simple condensation of resorcinol and an alkanedial, *Angew. Chem.* 118 (2006) 8116–8120.
- [35] G. Ye, J. Lee, F.O. Perreault, M. Elimelech, Controlled architecture of dual-functional block copolymer brushes on thin-film composite membranes for integrated “defending” and “attacking” strategies against biofouling, *ACS Appl. Mater. Interfaces* 7 (2015) 23069–23079.
- [36] A.K. Ghosh, E.M. Hoek, Impacts of support membrane structure and chemistry on polyamide-polysulfone interfacial composite membranes, *J. Membr. Sci.* 336 (2009) 140–148.
- [37] Z. Tan, S. Chen, X. Peng, L. Zhang, C. Gao, Polyamide membranes with nanoscale Turing structures for water purification, *Science* 360 (2018) 518–521.

- [38] P.W. Morgan, S.L. Kwolek, Interfacial polycondensation. II. Fundamentals of polymer formation at liquid interfaces, *J. Polym. Sci.* 40 (1959) 299–327.
- [39] Y. Ren, J. Zhu, S. Cong, J. Wang, B. Van der Bruggen, J. Liu, Y. Zhang, High flux thin film nanocomposite membranes based on porous organic polymers for nanofiltration, *J. Membr. Sci.* 585 (2019) 19–28.
- [40] Y. Li, X. You, Y. Li, J. Yuan, J. Shen, R. Zhang, H. Wu, Y. Su, Z. Jiang, Graphene quantum dot engineered ultrathin loose polyamide nanofilms for high-performance nanofiltration, *J. Mater. Chem. A* 8 (2020) 23930–23938.
- [41] V. Freger, Nanoscale heterogeneity of polyamide membranes formed by interfacial polymerization, *Langmuir* 19 (2003) 4791–4797.
- [42] J. Tian, P.K. Thallapally, S.J. Dalgarno, P.B. McGrail, J.L. Atwood, Amorphous molecular organic solids for gas adsorption, *Angew. Chem.* 121 (2009) 5600–5603.
- [43] M.B.M.Y. Ang, Y.-L. Ji, S.-H. Huang, K.-R. Lee, J.-Y. Lai, A facile and versatile strategy for fabricating thin-film nanocomposite membranes with polydopamine-piperazine nanoparticles generated in situ, *J. Membr. Sci.* 579 (2019) 79–89.
- [44] Y.-L. Ji, W.-J. Qian, Q.-F. An, S.-H. Huang, K.-R. Lee, C.-J. Gao, Mussel-inspired zwitterionic dopamine nanoparticles as building blocks for constructing salt selective nanocomposite membranes, *J. Membr. Sci.* 572 (2019) 140–151.
- [45] Z. Yao, H. Guo, Z. Yang, W. Qing, C.Y. Tang, Preparation of nanocavity-contained thin film composite nanofiltration membranes with enhanced permeability and divalent to monovalent ion selectivity, *Desalination* 445 (2018) 115–122.
- [46] S. Xiong, D.Y. Zhang, S. Mei, J. Liu, Y.S. Shi, Y. Wang, Thin film composite membranes containing intrinsic CD cavities in the selective layer, *J. Membr. Sci.* 551 (2018) 294–304.
- [47] Z. Zhang, N. Li, Y. Sun, H. Yang, X. Zhang, Y. Li, G. Wang, J. Zhou, L. Zou, Z. Hao, Interfacial force-assisted in-situ fabrication of graphene oxide membrane for desalination, *ACS Appl. Mater. Interfaces* 10 (2018) 27205–27214.
- [48] Y. Zeng, L. Wang, L. Zhang, J.Q. Yu, An acid resistant nanofiltration membrane prepared from a precursor of poly (s-triazine-amine) by interfacial polymerization, *J. Membr. Sci.* 546 (2018) 225–233.
- [49] J. Zhu, S. Yuan, A. Uliana, J. Hou, J. Li, X. Li, M. Tian, Y. Chen, A. Volodin, B. Van der Bruggen, High-flux thin film composite membranes for nanofiltration mediated by a rapid co-deposition of polydopamine/piperazine, *J. Membr. Sci.* 554 (2018) 97–108.
- [50] S. Yang, J. Wang, L. Fang, H. Lin, F. Liu, C.Y. Tang, Electrosprayed polyamide nanofiltration membrane with intercalated structure for controllable structure manipulation and enhanced separation performance, *J. Membr. Sci.* 602 (2020) 117971.
- [51] X. Li, C. Liu, W. Yin, T.H. Chong, R. Wang, Design and development of layer-by-layer based low-pressure antifouling nanofiltration membrane used for water reclamation, *J. Membr. Sci.* 584 (2019) 309–323.
- [52] L. Chen, J.-H. Moon, X. Ma, L. Zhang, Q. Chen, L. Chen, R. Peng, P. Si, J. Feng, Y. Li, High performance graphene oxide nanofiltration membrane prepared by electrospraying for wastewater purification, *Carbon* 130 (2018) 487–494.
- [53] Y.-S. Guo, Y.-L. Ji, B. Wu, N.-X. Wang, M.-J. Yin, Q.-F. An, C.-J. Gao, High-flux zwitterionic nanofiltration membrane constructed by in-situ introduction method for monovalent salt/antibiotics separation, *J. Membr. Sci.* 593 (2020) 117441.
- [54] Y.-S. Guo, X.-D. Weng, B. Wu, Y.-F. Mi, B.-K. Zhu, Y.-L. Ji, Q.-F. An, C.-J. Gao, Construction of nonfouling nanofiltration membrane via introducing uniformly tunable zwitterionic layer, *J. Membr. Sci.* 583 (2019) 152–162.
- [55] C. Boo, Y. Wang, I. Zucker, Y. Choo, C.O. Osuji, M. Elimelech, High performance nanofiltration membrane for effective removal of perfluoroalkyl substances at high water recovery, *Environ. Sci. Technol.* 52 (2018) 7279–7288.
- [56] Y. Kang, M. Obaid, J. Jang, I.S. Kim, Sulfonated graphene oxide incorporated thin film nanocomposite nanofiltration membrane to enhance permeation and antifouling properties, *Desalination* 470 (2019) 114125.
- [57] Y. Xiao, W. Zhang, Y. Jiao, Y. Xu, H. Lin, Metal-phenolic network as precursor for fabrication of metal-organic framework (MOF) nanofiltration membrane for efficient desalination, *J. Membr. Sci.* 624 (2021) 119101.
- [58] D. Qin, G. Huang, D. Terada, H. Jiang, M.M. Ito, A.H. Gibbons, R. Igashiri, D. Yamaguchi, M. Shirakawa, E. Sivaniah, Nanodiamond mediated interfacial polymerization for high performance nanofiltration membrane, *J. Membr. Sci.* 603 (2020) 118003.
- [59] Y. Qin, H. Liu, Y. Liu, M. Chen, K. Chen, Y. Huang, C. Xiao, Design of a novel interfacial enhanced GO-PA/APVC nanofiltration membrane with stripe-like structure, *J. Membr. Sci.* 604 (2020) 118064.
- [60] F.-Y. Zhao, Q.-F. An, Y.-L. Ji, C.-J. Gao, A novel type of polyelectrolyte complex/MWCNT hybrid nanofiltration membranes for water softening, *J. Membr. Sci.* 492 (2015) 412–421.
- [61] H. Zhang, Y. Wan, J. Luo, S.B. Darling, Drawing on membrane photocatalysis for fouling mitigation, *ACS Appl. Mater. Interfaces* 13 (2021) 14844–14865.